 CMES, vol.12, no.2, pp.121-136, 2006

A Meshless Spatial Coupling Scheme for Large-scale Fluid-structure-interaction Problems

R. Ahrem[1], A. Beckert[2], and H. Wendland[3]

Abstract: We present a new efficient scheme for loose coupling in fluid-structure-interaction problems as they typically appear in the context of aircraft design. This coupling scheme is based upon a multivariate scattered data interpolation approach, based on radial basis functions and partition of unity methods. It allows us to couple arbitrary meshes on fluid and structure side. It conserves virtual work and forces. It is designed for large scale problems and allows the coupling of entire aircraft meshes.

1 Introduction

In fluid-structure interaction (FSI) the reciprocal action of a flexible structure with a flowing fluid, in which it is submersed or by which it is surrounded, is studied. Naturally, FSI has applications in many fields of engineering, such as the stability and response of aircrafts, the flow of blood through arteries, the vibration of turbine and compressor blades, and the response of bridges and tall buildings to winds.

In this paper we study the mutual interaction between aerodynamical and elastic forces for an aerospace vehicle. An airborne aircraft structure is subjected to surface pressures induced by its surrounding flow. For an introduction into the field of *aeroelasticity* we refer the reader for example to Bisplinghoff and Ashley (1962); Fung (1955); Försching (1974); Dowell, Crawley, Jr., Peter, Scanlan, and Sisto (1995).

In the development process of future air vehicles, multidisciplinary simulation has become a key technology. For the design and clearance of modern aircrafts, such multi-disciplinary simulations are used to predict and to analyze the behavior of the elastic aircraft in flight and during maneuver (Geuzaine, Brown, Harris, and Farhat (2003); Fornasier, Rieger, Tremel, and der Weide (2002)). This is particularly crucial for highly critical flight conditions representing specific parts of the flight envelope. The behavior of the elastic aircraft in flight is influenced by the interaction between deformations of the elastic structure caused by fluid flow and the impact of the aerodynamic forces on the structure. Hence, the interaction between the fluid flow and the elastic structure has to be studied in depth (Done (1996); Edward (1993); Försching (1994, 1995)).

In principle, there are two different approaches to the numerical solution of FSI problems. In a *monolithic* approach, one tries to model the fluid, the structure, and the interaction in one *single* model. While this has from the mathematical point of view certain advantages, its drawbacks in practical applications come in particular from the fact that the new mathematical model forces a completely new programming of the solver. In particular, for complex aeroelastic problems, the fluid and the structural domain show different mathematical and numerical properties, requiring highly tuned and adapted solvers. Hence, the simultaneous solution by a monolithic scheme is in general computationally challenging, mathematically and economically suboptimal, and software-wise almost unmanageable (Farhat and Lesoinne (1998)).

A more practical point of view is taken in the *loose coupling* approach. Here, for each time step, the fluid and the structural problem are solved independently, and the influence of the other problem is restricted to the exchange of boundary conditions. To be more precise, a loose coupling scheme consists mainly of the iteration of the following four steps:

1. Compute the fluid solution and the resulting forces on fluid side.
2. Transfer the forces to the structure.
3. Compute the solution of the structure problem resulting in displacements on the structural side.

[1] Institut für Numerische und Angewandte Mathematik, Universität Göttingen
[2] European Aeronautic Defence and Space Company (EADS)
[3] Institut für Numerische und Angewandte Mathematik, Universität Göttingen

4. Transfer the deformations to the fluid model.

This has the important advantage that problem-specific models and existing solvers for both the fluid and the structure problem can still be used in FSI. However, since now we cannot expect the underlying discretizations of the single problems to match, special methods have to be developed to exchange these boundary conditions.

In this paper we will concentrate on this interface problem and describe a procedure which allows us to couple *arbitrary* meshes. In fact, the discretizations do not even have to be based upon a *mesh*, since our coupling procedure is using only point-based information. Our method will be based upon radial basis function interpolation. Recent reviews on meshless scattered data methods can, for example, be found in Atluri (2004, 2005); Atluri and Shen (2005); Buhmann (2001); Wendland (2005).

This paper is organized as follows. In the next section, we describe the three field formulation for a typical FSI problem. The third section is devoted to our coupling scheme, where special emphasis is put on efficiency and the conservation of virtual work and forces. The final section deals with a real-world example. Our coupling scheme is applied to the spatial coupling of an entire aircraft model. We also compare our method to other ones previously used.

2 The Three Field Formulation

Fluid-structure-interaction problems are generally described in a so called three field formulation, referring to the fluid domain, the structural domain and the interface between both of them.

To be more precise, let $\Omega(t)$ be a time dependent domain of $\mathbb{R}^3$. We will assume that $\overline{\Omega(t)} = \overline{\Omega_F(t)} \cup \overline{\Omega_S(t)}$ for all time and $\Omega_F(t) \cap \Omega_S(t) = \emptyset$. Here, $\Omega_F(t)$ denotes the domain occupied by the fluid at time t, while $\Omega_S(t)$ denotes the structural domain. Finally, let $\Gamma(t) = \overline{\Omega_F(t)} \cap \overline{\Omega_S(t)}$ be the fluid-structure interface.

On $\Omega_F(t)$ the governing equations that describe the flow are given by the Navier-Stokes or Euler equations. These equations are based on the conservation of mass, momentum, and energy. In our application, we will restrict ourselves to the Euler equations for compressible flow,

$$\frac{\partial \rho}{\partial t} + \nabla \cdot (\rho \mathbf{u}) = 0 \tag{1}$$

$$\frac{\partial (\rho \mathbf{u})}{\partial t} + \nabla \cdot (\rho \mathbf{u})\mathbf{u} + \nabla p = 0 \tag{2}$$

$$\frac{\partial (\rho E)}{\partial t} + \nabla \cdot (\rho \mathbf{u}(E+p)) = 0 \tag{3}$$

coming from the conservation of mass (1), of momentum (2), and energy (3).

Here, $\mathbf{u}$ denotes the velocity field, p the pressure, ρ the density, and $E = \rho e + \rho \|\mathbf{x}\|_2^2/2$ the energy (where e is the internal energy and $\mathbf{x} \in \mathbb{R}^3$ the position vector). If, in addition, T denotes the temperature then these unknowns are related by an equation of state which, for atmospheric flight conditions, is the perfect gas law

$$\frac{p}{\rho} = RT[1+\alpha], \tag{4}$$

where $\alpha = \alpha(p,T)$ is an effective mass fraction of diatomic molecules in the dissociated condition and R is the "undissociated" gas constant. If dissociation is neglected, then (4) implies that the specific internal energy, e, and *enthalpy*

$$h = e + \frac{p}{\rho} \tag{5}$$

are functions of T only, which can be expressed by the caloric equation of state for a calorically perfect gas:

$$e = c_v T. \tag{6}$$

For more details see for example Bisplinghoff and Ashley (1962).

In our application, theses equations have to be solved in the outer field around an aircraft, i.e. $\Omega_F(t) = \mathbb{R}^3 \setminus \overline{\Omega_S(t)}$.

The solution of the Euler equations produces a pressure distribution on the structure, from which forces result, which act on the structure (in the case of an aircraft they are responsible for the lift). However, for elastic structures these forces lead also to a deformation of (parts) of the structure, which, in practical computations, cannot be neglected.

These deformations are typically described by the Lamé or Navier-Cauchy equations

$$\rho \ddot{\mathbf{s}} = \mu \Delta \mathbf{s} + (\mu + \lambda) \nabla (\nabla \cdot \mathbf{s}) + \mathbf{b}, \tag{7}$$

where λ and μ are the Lamé constants and represent the elastic properties of the structure, $\mathbf{s}$ is the displacement

field, **b** are the body and external forces, and ρ is the density of the body.

In particular in aeroelastic computations, an eigenmode formulation of (7) is used. Suppose the displacements **s** are expressed as

$$\mathbf{s}(\mathbf{x},t) = \sum_{n=1}^{\infty} q_n(t)\boldsymbol{\psi}_n(\mathbf{x}),$$

where the functions $\boldsymbol{\psi}_n(\mathbf{x})$ are the natural eigenmodes of vibration of the structure and $q_n(t)$ are the Lagrange variables. Then, using only a finite number of Lagrange variables, (7) can be expressed as

$$\sum_{p=1}^{N} M_{np}\ddot{q}_p(t) + \sum_{p=1}^{N} K_{np}q_p(t) \quad = \quad e_n \tag{8}$$

for $1 \leq n \leq N$, where $M = (M_{np})$ is the mass and $K = (K_{np})$ the stiffness matrix, and e_n results from the body and external forces.

Both problems have to be completed by appropriate boundary and initial conditions. However, in the context of FSI problems (some of) these boundary conditions are given by the other problem. To be more precise, on $\Gamma(t)$ we have to transfer

- forces from the fluid problem, which are integrated pressures, to the structural domain,
- displacements, resulting from the structural solver, to the fluid domain.

This has to be done in a conservative way, such that virtual work and forces are globally preserved. We will describe this exchange of boundary conditions only for already discretized problems.

It is important to see that discretized models of the fluid and structural problem differ in almost all practical applications. First of all, already the continuous model differ, since, in general, the Navier-Stokes or Euler equations are described in Eulerian coordinates while the structural problem is designed using Lagrangian coordinates. Moreover, often, finite volume schemes are used to discretize the fluid problem while finite element methods dominate discretization schemes for the structural problem.

3 The Coupling Procedure

We will now describe our coupling procedure. This means that we have to describe two steps in the coupling process. The first step is concerned with transferring displacement vectors from the structural grid to the aerodynamical mesh, while the second step deals with transferring forces from the aerodynamical mesh to the structural one. Our coupling scheme will be based only upon *point information* giving the most possible flexibility.

To make this more precise we will from now on use the following notation:

- Structural side:
  - $X = \{\mathbf{x}_1, \ldots, \mathbf{x}_N\}$ is the set of nodes,
  - $\mathbf{f} = (\mathbf{f}(\mathbf{x}_1), \ldots, \mathbf{f}(\mathbf{x}_N))$ are the forces that have to be computed during the coupling process,
  - $\mathbf{g} = (\mathbf{g}(\mathbf{x}_1), \ldots, \mathbf{g}(\mathbf{x}_N))$ are the displacements that are given by the structural solver.
- Aerodynamical side:
  - $Y = \{\mathbf{y}_1, \ldots, \mathbf{y}_M\}$ is the set of nodes,
  - $\mathbf{F} = (\mathbf{F}(\mathbf{y}_1), \ldots, \mathbf{F}(\mathbf{y}_M))$ are the forces that are computed by the fluid solver,
  - $\mathbf{G} = (\mathbf{G}(\mathbf{y}_1), \ldots, \mathbf{G}(\mathbf{y}_M))$ are the displacements that have to be computed during the coupling process.

Note that the involved forces and displacements $\mathbf{f}(\mathbf{x}_j), \mathbf{g}(\mathbf{x}_j), \mathbf{F}(\mathbf{y}_j)$, and $\mathbf{G}(\mathbf{y}_j)$ are $3D$ vectors. Hence, from now on $\mathbf{f}_i = (f_i(\mathbf{x}_1), \ldots, f_i(\mathbf{x}_N))^T \in \mathbb{R}^N$ denotes the ith component of the Matrix **f**, and so on.

3.1 Exchanging Forces

The entire coupling process can be described by employing a *coupling matrix* $H \in \mathbb{R}^{M\times N}$, which relates the displacement vectors via

$$\mathbf{G}_i = H\mathbf{g}_i, \qquad 1 \leq i \leq 3. \tag{9}$$

We will discuss how to derive such a coupling matrix in the next subsection. But for the time being, let us assume that we have such a coupling matrix $H \in \mathbb{R}^{M\times N}$ at hand. Then, we can use H also to exchange the forces simply by setting

$$\mathbf{f}_i = H^T\mathbf{F}_i, \qquad 1 \leq i \leq 3. \tag{10}$$

This simple approach already guarantees conservation of virtual work and has been used often before (see for example Beckert (2000); Harder and Desmarais (1972); Hounjet and Meijer (1994)). However, to conserve also forces, the following terminology will prove to be useful.

Definition 3.1. *A coupling matrix $H \in R^{M\times N}$ will be called* conservative *if*

$$H\mathbf{e}_N = \mathbf{e}_M$$

where the k-dimensional vector $\mathbf{e}_k$ is given by $\mathbf{e}_k = (1,\ldots,1)^T \in \mathbb{R}^k$.

For *any* coupling process of the form (9) and (10) it is true that the virtual work is conserved. This, and the conservation of forces is subject of

Theorem 3.2. *Suppose the coupling process is based upon the coupling matrix $H \in \mathbb{R}^{M\times N}$ via (9) and (10). Then, it conserves virtual work:*

$$\sum_{j=1}^{N} f_i(\mathbf{x}_j)g_i(\mathbf{x}_j) = \sum_{j=1}^{M} F_i(\mathbf{y}_j)G_i(\mathbf{y}_j), \qquad 1 \le i \le 3.$$

Moreover, if the coupling matrix H is conservative in the sense of Definition 3.1, then the coupling process also conserves forces:

$$\sum_{j=1}^{N} f_i(\mathbf{x}_j) = \sum_{j=1}^{M} F_i(\mathbf{y}_j), \qquad 1 \le i \le 3.$$

Proof. For the first part, one simply has to realize that

$$\mathbf{f}_i^T\mathbf{g}_i = (H^T\mathbf{F}_i)^T\mathbf{g}_i = \mathbf{F}_i^T H\mathbf{g}_i = \mathbf{F}_i^T\mathbf{G}_i$$

for any $1 \le i \le 3$. The conservation of forces follows in the same way. Since our coupling matrix H is supposed to be conservative, we have

$$\begin{aligned}\sum_{j=1}^{N} f_i(\mathbf{x}_j) &= \mathbf{f}_i^T\mathbf{e}_N = (H^T\mathbf{F}_i)^T\mathbf{e}_N \\ &= \mathbf{F}_i^T H\mathbf{e}_N = \mathbf{F}_i^T\mathbf{e}_M = \sum_{j=1}^{M} F_i(\mathbf{y}_j)\end{aligned}$$

for $1 \le i \le 3$. □

While a conservative coupling matrix has the just stated conservation properties which are crucial to any coupling process, the global approach using (10) depends heavily on the choice of the coupling matrix H. For example, a global coupling matrix H built with radial basis functions as proposed in Hounjet and Meijer (1994); Beckert and Wendland (2001) leads often to an undesired and unphysical distribution of forces on the structural side. Our new local method will also remedy this kind of problem.

3.2 Exchanging Displacements

In this section we describe how the coupling matrix H can generally be built. This is done in the context of *scattered data interpolation*, where only node information is required such that the coupling can be carried out between arbitrary meshes.

To be more precise, to transfer displacements from the structural model to the aerodynamical model we first assume that each coordinate of the displacement field can be modeled independently. This assumption is problematic if additional information like rotations are given, but it is appropriate as long as the deformations are small. However, our approach can also be generalized to incorporating rotations. But we will not pursue this here.

A radial basis function interpolant is a function of the form

$$s(\mathbf{x}) = \sum_{j=1}^{N} \alpha_j\Phi(\mathbf{x}-\mathbf{x}_j) + p(\mathbf{x}).$$

Here, $\Phi : \mathbb{R}^3 \to \mathbb{R}$ is a (conditionally) positive definite function of a certain order m and $p \in \pi_{m-1}(\mathbb{R}^3)$ is a 3-variate polynomial of degree at most $m-1$. The coefficient vector $\boldsymbol{\alpha} \in \mathbb{R}^N$ as well as the polynomial p are determined by the interpolation conditions

$$s(\mathbf{x}_j) = v_j, \qquad 1 \le j \le N,$$

where $v_j = g_i(x_j)$ are the given deformation for the ith coordinate (i between 1 and 3 is from now on considered fixed) together with the additional conditions

$$\sum_{j=1}^{N} \alpha_j q(\mathbf{x}_j) = 0, \qquad \text{for all } q \in \pi_{m-1}(\mathbb{R}^3).$$

Typical examples of radial basis functions together with their order m are given in Table 1. The names are abbreviations for *Volume Spline, Thin-Plate Spline, Multi-Quadric, Inverse Multi-Quadric, Gaussian, Wendland C0, C2, C4, and Euclid's Hat*, respectively. For W1–W3 and EH we used the notation $(r)_+ = \max\{0, r\}$. Hence,

Table 1 : Conditionally positive definite functions

$\Phi(\mathbf{x}) = \phi(r)$ with $r = \|\mathbf{x}\|_2$	Name	CPD
r	VS	$m \geq 1$
$r^2 \log r$	TPS	$m \geq 2$
$\sqrt{r^2+1}$	MQ	$m \geq 1$
$1/\sqrt{r^2+1}$	IMQ	$m \geq 0$
$\exp(-r^2)$	G	$m \geq 0$
$(1-r)_+^2$	W1	$m \geq 0$
$(1-r)_+^4(1+4r)$	W2	$m \geq 0$
$(1-r)_+^6(35r^2+18r+3)$	W3	$m \geq 0$
$\frac{\pi}{12}(r+2)(1-r)_+^2$	EH	$m \geq 0$.

W1–W3 and EH have a compact support. The support radius can be simply changed by scaling $\phi(\cdot/\delta)$. Note that these compactly supported functions are only positive definite on $\mathbb{R}^d$ with $d \leq 3$, which is sufficient for our purposes, while all the others are conditionally positive definite on *every* $\mathbb{R}^d$. More information on the theoretical background can be found in Wendland (2005). Here, only two things matter. First, a smoother basis function leads to a smother displacement field and hence to a more realistic deformation. But a smoother basis function often also suffers from numerical instability. Hence, the function should be chosen as smooth as possible, depending on the given data set.

Second, a conditionally positive definite function of order m is also conditionally positive definite of order $\ell > m$. In particular, in the case of an unconditionally positive definite function, where no polynomial part for the interpolant is necessary, it does not harm to add a polynomial part. On the contrary, in the light of Definition 3.1 all computations should be done using at least a constant polynomial.

The resulting coupling matrix can be set up in the following way. Suppose $p_1, \ldots, p_Q$ form a basis for the space of polynomials $\pi_{m-1}(\mathbb{R}^3)$. Define $A_{\Phi,X} = (\Phi(\mathbf{x}_j - \mathbf{x}_k)) \in \mathbb{R}^{N\times N}$ and $P_X = (p_j(\mathbf{x}_i)) \in \mathbb{R}^{N\times Q}$. Then, the coefficient vector $\boldsymbol{\alpha}$ can, together with the coefficient vector $\boldsymbol{\beta} \in \mathbb{R}^Q$ of $p = \sum_k \beta_k p_k$, be determined from the linear system

$$\begin{pmatrix} A_{\Phi,X} & P_X \\ P_X^T & \mathbf{0} \end{pmatrix} \begin{pmatrix} \boldsymbol{\alpha} \\ \boldsymbol{\beta} \end{pmatrix} = \begin{pmatrix} \mathbf{v} \\ \mathbf{0} \end{pmatrix} \tag{11}$$

It is well known (cf. Wendland (2005)) that the linear system (11) has a *unique* solution provided Φ is conditionally positive definite of order m and provided that the set X is $\pi_{m-1}(\mathbb{R}^d)$ unisolvent. The latter means that the only polynomial from $\pi_{m-1}(\mathbb{R}^d)$ vanishing on X is the zero polynomial.

If we additionally define, for given evaluation points $Y = \{\mathbf{y}_1 \ldots, \mathbf{y}_M\} \subseteq \Omega$, the matrices $A_{\Phi,X,Y} = (\Phi(\mathbf{y}_i - \mathbf{x}_j)) \in \mathbb{R}^{M\times N}$ and $P_Y = p_j(\mathbf{y}_i) \in \mathbb{R}^{M\times Q}$, then we can read off the coupling matrix $H : \mathbb{R}^N \to \mathbb{R}^M$ from

$$\begin{aligned} s|Y &= \begin{pmatrix} A_{\Phi,X,Y} & P_Y \end{pmatrix} \begin{pmatrix} A_{\Phi,X} & P_X \\ P_X^T & \mathbf{0} \end{pmatrix}^{-1} \begin{pmatrix} \mathbf{v} \\ \mathbf{0} \end{pmatrix} \\ &=: \begin{pmatrix} H & \widetilde{H} \end{pmatrix} \begin{pmatrix} \mathbf{v} \\ \mathbf{0} \end{pmatrix} \end{aligned} \tag{12}$$

Hence, for small data sets the coupling matrix H can be precomputed and, in each step of the iterative coupling algorithm, the deformations and also the forces can be exchanged by a simple matrix by vector multiplication.

The resulting coupling matrix is indeed conservative as long as constant polynomials are added to the interpolant. Thus, this must (and indeed can) be done also for (unconditionally) positive definite functions.

Lemma 3.3. *Suppose the interpolation process by radial basis function employs at least a constant polynomial (i.e. $m \geq 1$). Suppose further that the data sites are $\pi_{m-1}(\mathbb{R}^3)$ unisolvent. Then, the resulting coupling matrix is conservative and the coupling (9) and (10) preserves virtual work and forces.*

Proof. In the light of Theorem 3.2 it suffices to show that the resulting coupling matrix H is conservative. However, since the interpolant is unique, polynomials from $\pi_{m-1}(\mathbb{R}^3)$ are exactly recovered. This means that if the data values are generated by such a polynomial the interpolant is the polynomial. Hence, if we have $v_j = 1$ for $1 \leq j \leq N$, then the interpolant s is identical one, i.e. $s = 1$ meaning in particular $s(\mathbf{y}_j) = 1$ for all $1 \leq j \leq M$. But this means that H is conservative. □

Note that the proof actually leads to a stronger conservation property. Employing polynomials of degree $\pi_{m-1}(\mathbb{R}^d)$ leads to the moment condition

$$\sum_{j=1}^{N} f_i(\mathbf{x}_j) p(\mathbf{x}_j) = \sum_{j=1}^{M} F_i(\mathbf{y}_j) p(\mathbf{y}_j)$$

for $1 \leq i \leq 3$, $p \in \pi_{m-1}(\mathbb{R}^3)$.

So far we have mainly described the method from Beckert and Wendland (2001); Harder and Desmarais (1972), which has successfully been used for smaller models. However, problems arise if the size of the models becomes larger. This is mainly due to two facts. On the one hand, to compute the coupling matrix H we have to invert the $(N+Q)\times(N+Q)$ matrix in (11). Since Q is negligible when compared to N, the number of nodes on the structural side, this has an $O(N^3)$ complexity. Multiplying the matrix $\begin{pmatrix} \widetilde{A} & \widetilde{P} \end{pmatrix}$ with this inverse needs another $O(NM)$ operations. For N and M too large both operations, even if they have to be done only once, need too much time. Moreover, for large M and N it is also not reasonable, sometimes not even possible to keep the $M\times(N+Q)$ matrix H in the main memory of a modern computer. For example, if we have $N = 10,000$ structural nodes and $M = 1,000,000$ dynamical surface nodes, storing the matrix in `double` format using 8 bytes per number would need more than 74 gigabytes of memory.

Hence, for larger models it is necessary to design an enhanced coupling method for exchanging these data between the two models. We will achieve this here, by combining the radial basis function interpolation approach with a partition of unity, see Wendland (2002). The idea behind this method can be described as follows. First, a region of interest Ω is defined. This region must contain the node sets X and Y. Next, Ω is decomposed into a number of overlapping subregions: $\Omega \subseteq \cup_{j=1}^{K}\Omega_j$. This decomposition has to be done in such a way that each *patch* Ω_j contains only a small number N_j of points, which, when compared to N, can be considered to be constant. Consequently, the number of patches K has to be proportional to the number N. Moreover, it is important that each $y \in Y$ is contained in only a small number of patches and that these patches can be found fast. These requirements make it necessary to build "intelligent" data structures for both the points in X and the patches Ω_j.

For each patch Ω_j we collect the points from X in X_j, i.e. $X_j = X\cap\Omega$. Then, we solve the interpolation problem on each patch in the previously described way, resulting in a local interpolant s_j. Since the number of points in each X_j can be considered to be constant, this can be done in constant time for each patch and, since we have $O(N)$ patches the overall time is also $O(N)$ plus the time necessary to build the associated data structures. Such data structures are in general based upon binary trees and can be constructed in $O(N\log N)$ time. Finally, the global interpolant is now formed by weighting the local interpolants. To this end, a partition of unity is chosen. This is a family of smooth, nonnegative functions $\{w_j\}_{j=1}^{K}$ such that each w_j is supported only on its associated patch Ω_j, i.e. w_j vanishes outside Ω_j. Moreover, the weight functions are supposed to sum up to one:

$$\sum_{j=1}^{K} w_j(\mathbf{x}) = 1, \qquad \mathbf{x}\in\Omega.$$

Then, the global interpolant is formed by

$$s(\mathbf{x}) = \sum_{j=1}^{K} w_j(\mathbf{x}) s_j(\mathbf{x}).$$

It inherits many of the properties of the local interpolants. For example, it is really an interpolant and it preserves the approximation orders of the local interpolants. Moreover, if the constant number of patches that contain a single evaluation point can be located in $\log(N)$ time, which is the case for the above mentioned data structures, then each evaluation also takes only $\log(N)$ time.

The evaluation of the interpolant can, as in the global case (12) be described by a matrix vector multiplication. Using the transposed of this new coupling matrix for transferring forces from the aerodynamic to the structural model leads again to a conservative scheme.

Lemma 3.4. *Suppose that on each patch Ω_k the interpolation process employs at least a constant polynomial (i.e. $m \geq 1$) and that the local data sets $X_k = X\cap\Omega_k$ are $\pi_{m-1}(\mathbb{R}^d)$ unisolvent. Suppose finally that H is the resulting coupling matrix from our partition of unity approach. Then, H is conservative and the coupling scheme (9) and (10) preserves virtual work and forces.*

Proof. Given input data $\mathbf{e}_N = (1,\ldots,1)^T \in \mathbb{R}^N$ lead on every patch Ω_k to local input data $\mathbf{e}_{N_k}$, and hence to a local interpolant s_k which is identical one. Thus, the global interpolant s satisfies

$$s(\mathbf{x}) = \sum_k w_k(\mathbf{x}) s_k(\mathbf{x}) = \sum_k w_k(\mathbf{x}) = 1$$

for all $\mathbf{x}\in\Omega$, meaning that the coupling matrix is conservative. □

Employing such a local strategy has the additional advantage that forces and work are also locally preserved resulting automatically into a more local distribution of the forces, which will be demonstrated in the next section.

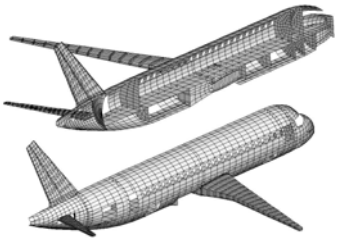

Figure 1 : The structural model

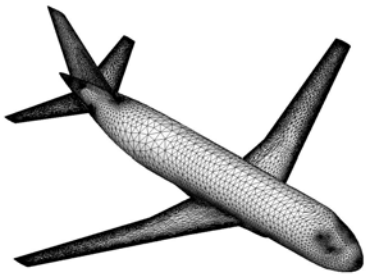

Figure 2 : The aerodynamical model

4 Numerical Results

In this section, we present computational results for the just described aeroelastic problem in the static aeroelastic equilibrium.

We applied our new coupling technique as well as the global one based only on radial basis functions to Alenia's SMJ model, which has been developed by Alenia Aeronautica and provided as a test case for the TAURUS project. It describes a reference for a 70 seats passenger aircraft.

4.1 Alenia's SMJ Model

The structural model consists of a fuselage, fixed in its plane of symmetry, a wing structure, and a horizontal and a vertical tail (see Figure 1). For the numerical computation of the static aeroelastic equilibrium of the aircraft, symmetric boundary conditions have been imposed.

The discretized model consists of 5630 nodes and 12 388 finite elements of different types. The structural finite element equations are solved by an analysis code using the formulation of the structural model in a generalized form. The related generalized coordinates, stiffness and mass matrices result from a normal-modes solution, which has been performed using the finite element analysis code MSC.Nastran (Msc (1987)).

For the aerodynamic model of the transport aircraft, the fluid flow is described by the nonlinear three-dimensional Euler equations. which are solved by a specific upwind-scheme based on finite volumes. In our situation, spatial discretization is given by an unstructured finite volume mesh consisting of four million tetrahedrons. The surface mesh of the complete aircraft (see Figure 2) is based on about 300 000 triangles.

Figure 3 : The difference between the structural and aerodynamical model

The difference between both models can best be seen from Figure 3. Obviously, there are large regions, in particular on the wings, where no structural information is available, which makes the coupling process difficult and causes standard projection methods to fail. As a matter of fact, any interpolation method turns into an extrapolation method.

4.2 Results of the Aeroelastic Analysis

In this section, we present the results of the aeroelastic analysis compared to a rigid nonelastic computation.

For simplicity, all computations were done with the CG (center of gravity) fixed. After convergence of the iteration was reached, the deflected shape showed a maximum vertical translation of 0.41 mt at the wing tip (upward) and a 0.15 mt downward deflection at the horizontal tailplane (see Figure 4).

The deformation of the structure leads to a decrease of the total lift as shown in Figure 5. Beside this decreased lift, a different behavior of the spanwise C_p distribution at the wing tip is given.

This phenomenon can be explained by a vortex at the trailing edge of the wing tip. In this region, the fluid particles undergo a rapid acceleration when passing the tip

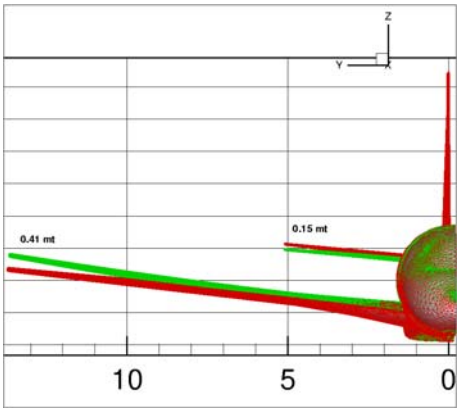

Figure 4 : Maximum deflections

and produce a local vortex that increases the Mach number to a maximum value of 1.4. Table 2 summarizes the differences between the elastic and rigid computations in terms of lift and drag. Clearly, the influence of the elasticity cannot be neglected.

Table 2 : Influence of elasticity

	elastic	rigid	Δ%
Lift C_l	0.431	0.508	-15
Drag C_d	0.0299	0.0368	-18

4.3 Comparison of the PoU and the Global Coupling Method

We will now compare the global coupling method based on RBF interpolation with the local method using also a partition of unity. Moreover, we analyze the influence of the employed radial basis function. Significant differences in the interpolated displacement fields result into undesired different aerodynamical models and eventually into different aeroelastic equilibriums. Hence, to avoid ambiguity a method which is indifferent with respect to the chosen basis function is preferable.

In detail, our comparison is based upon the following quantities:

- Vertical translation along wing span
- Pressure distribution
- Variation of sweep angle (i.e. local angle of attack)

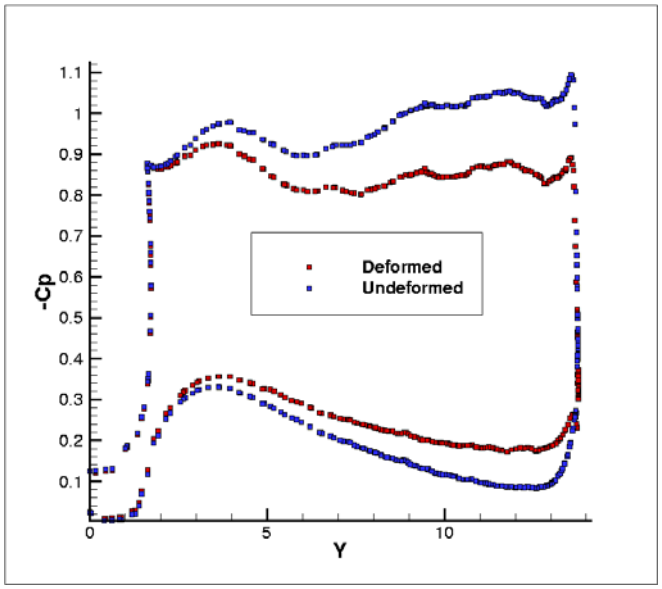

Figure 5 : Pressure Distribution

- Load distribution
- Computational time
- Boundary effects

4.3.1 Vertical Translation

We start with the vertical translation along the wing span. The results for different basis functions are shown in Figure 6 for the global method and in Figure 7 for the PoU method. The maximum difference between the basis functions is 7.5% in the global and 0.5% in the local setting. Hence, the local method produces more reliable results being almost independent of the chosen radial basis function.

4.3.2 Pressure Distribution

Next we take a look at the pressure distribution. Figures 8 to 12 show the results for the global method and different basis functions. The results for the local method are presented in Figures 13 to 17. Again, in the case of the global method significant differences appear. For example, in the area of the wing near its root (where most of the lift is generated), the results for W2 and TPS are quite different, in particular where the flow expands behind the leading edge. Moreover, in the case of TPS, there is a thin region of low pressure, which is parallel to the wing axis and extends from the tip to the mid span.

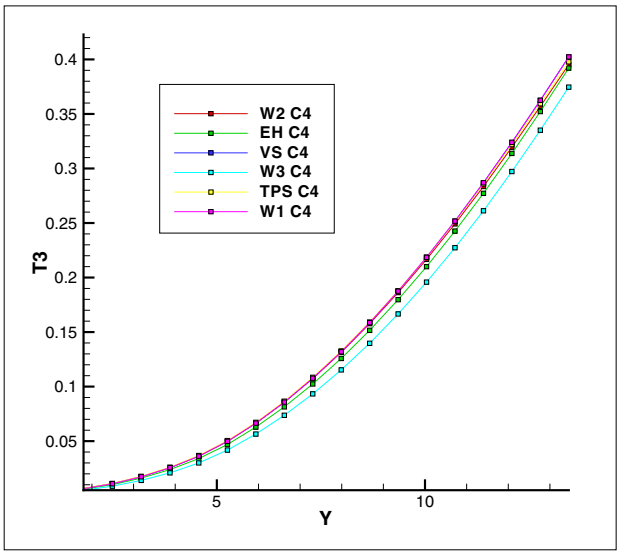

Figure 6 : Influence of the chosen RBF on the global method

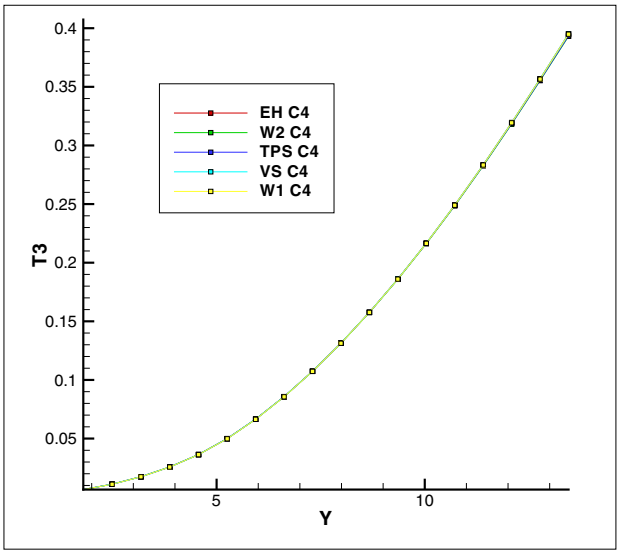

Figure 7 : Influence of the chosen RBF on local method

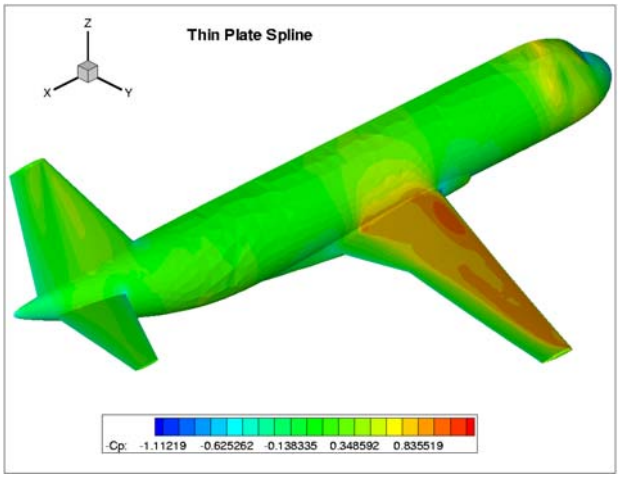

Figure 8 : Pressure distribution, global, TPS

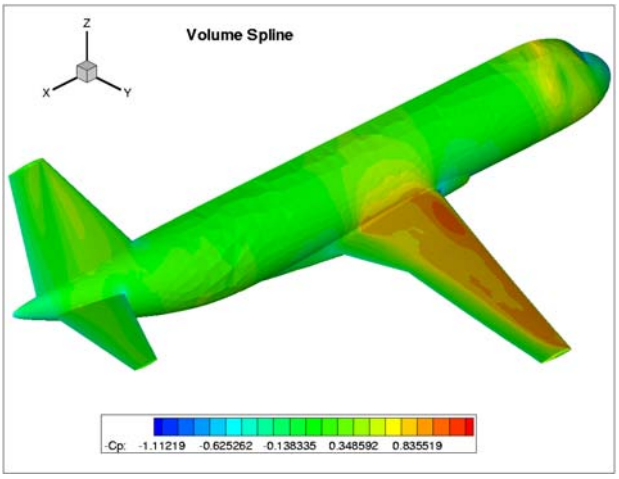

Figure 9 : Pressure distribution, global, VS

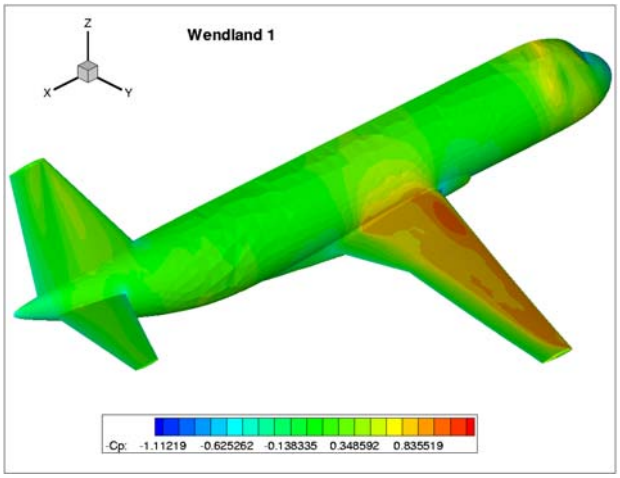

Figure 10 : Pressure distribution, global, W1

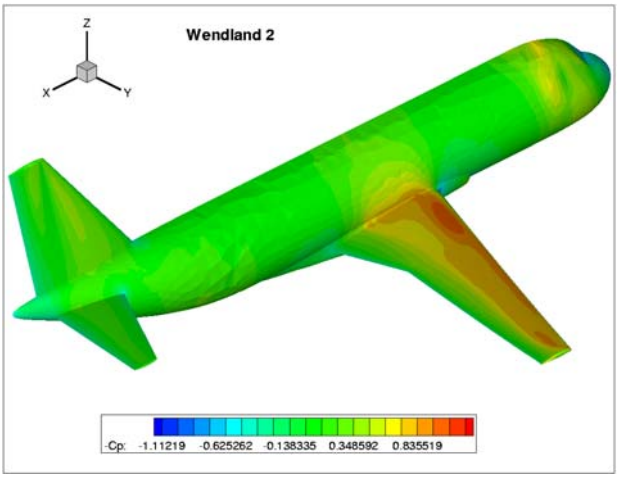

Figure 11 : Pressure distribution, global, W2

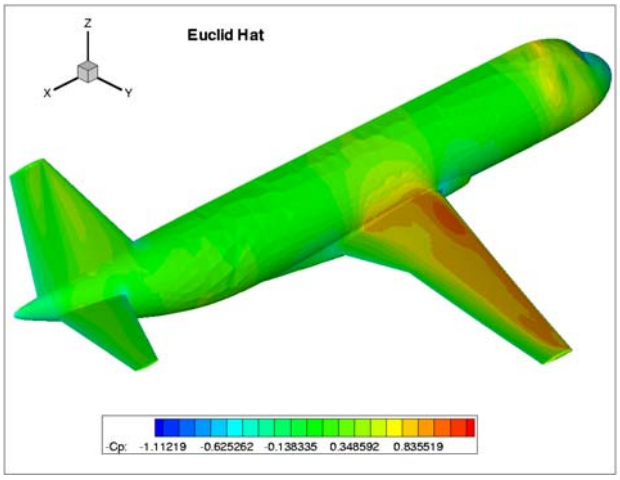

Figure 12 : Pressure distribution, global, EH

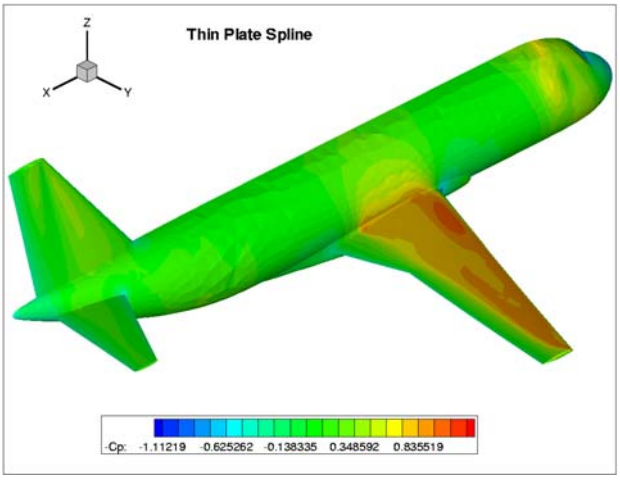

Figure 13 : Pressure distribution, PoU, TPS

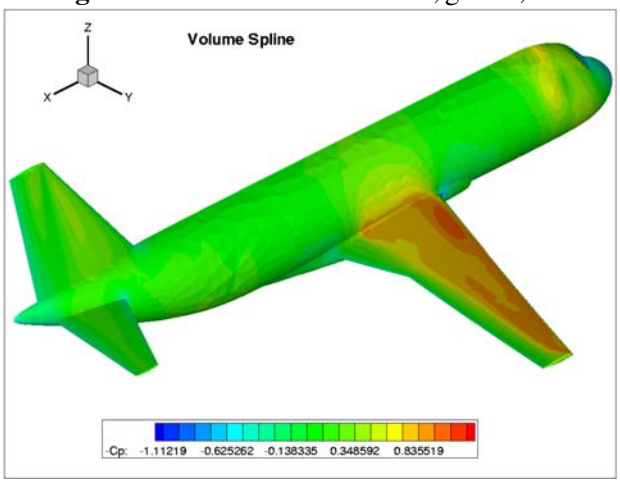

Figure 14 : Pressure distribution, PoU, VS

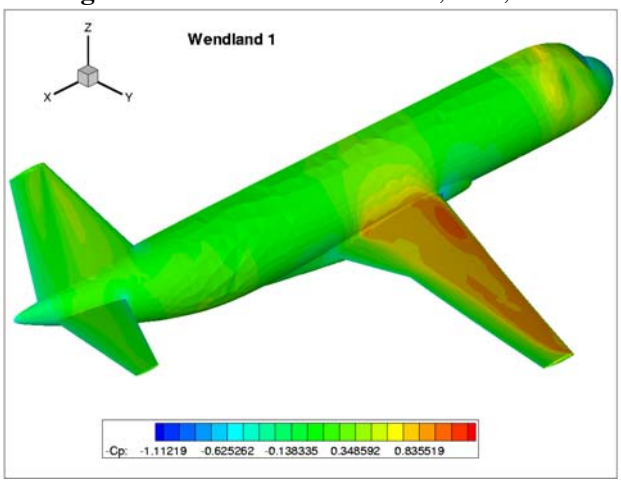

Figure 15 : Pressure distribution, PoU, W1

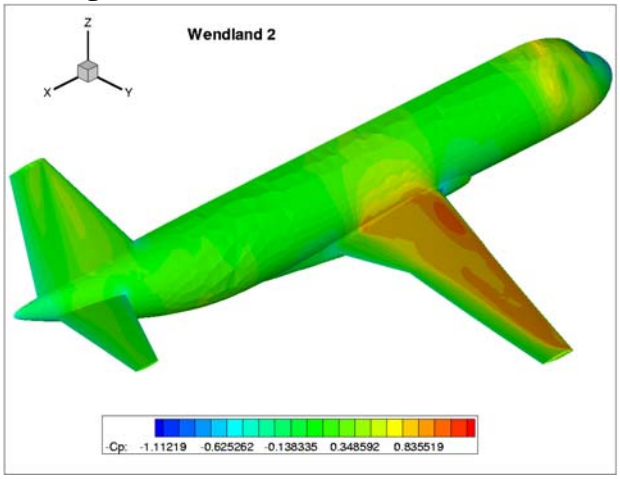

Figure 16 : Pressure distribution, PoU, W2

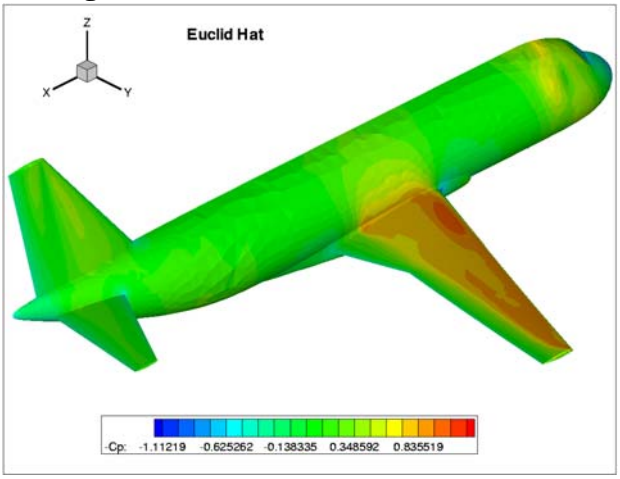

Figure 17 : Pressure distribution, PoU, EH

This region does not appear in the case of the other basis functions. But it is visible for all basis functions in the case of the local method. Moreover, again, the pressure distribution is almost independent of the employed basis function.

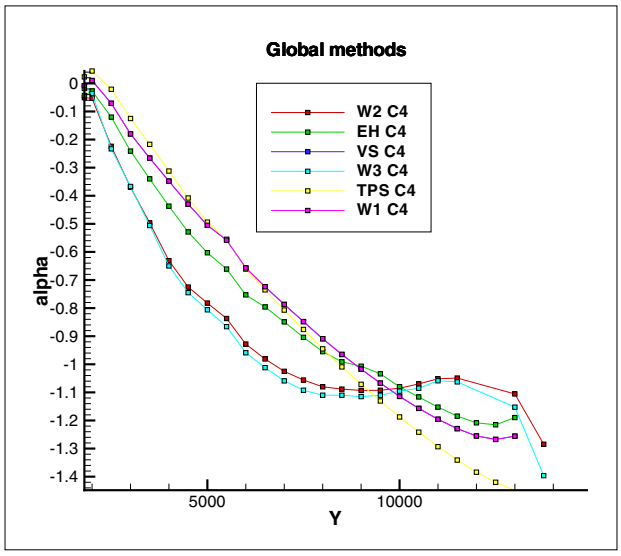

Figure 18 : Angle of Attack: Global method

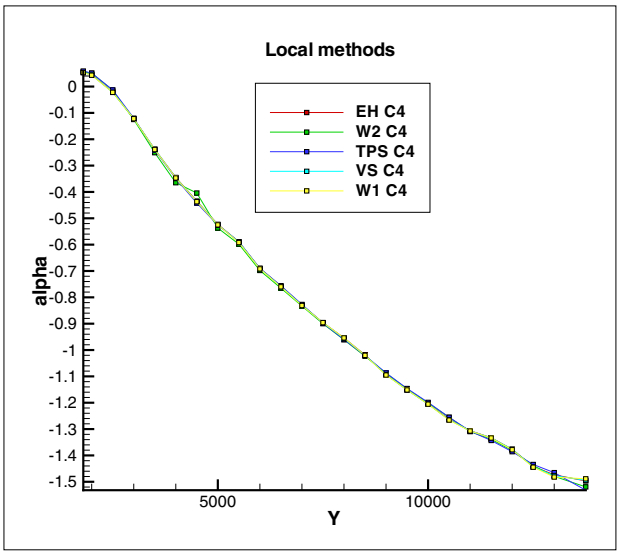

Figure 19 : Angle of Attack: PoU method

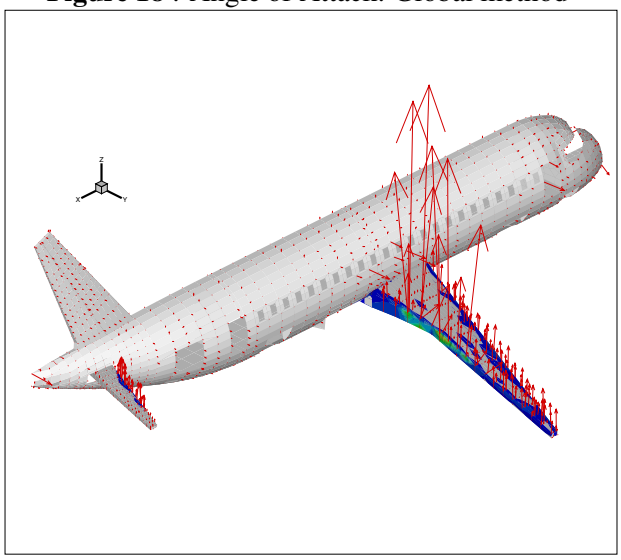

Figure 20 : Transformed forces on the FE model, global method

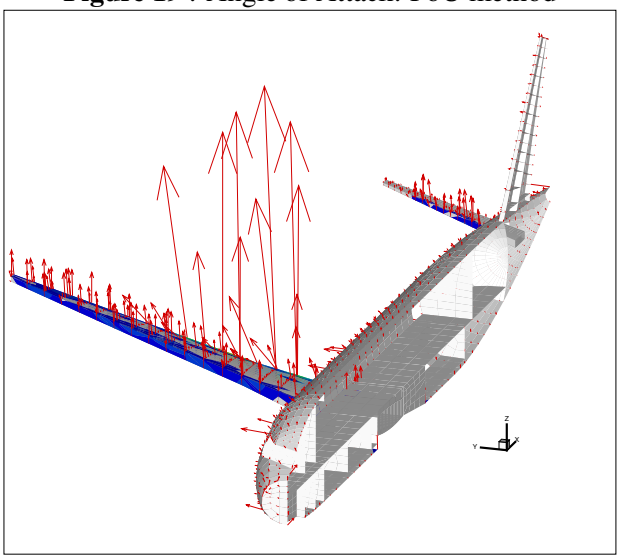

Figure 21 : Transformed forces on the FE model, global method

4.3.3 Variation of the Local Angle of Attack

In order to analyze the torsional deformation of the wing in terms of a local angle of attack, we used a linear interpolation between the vertical displacements of points at the LE (leading edge) and the corresponding points at the TE (trailing edge). The results are presented in Figures 18 and 19 and confirm once again that the global method is significantly dependent on the underlying basis function. In particular for smoother basis functions (W2 and W3), the angle of attack represents a curve with a higher concavity and, when approaching the wing tip, the slope of the curve changes even its sign (at around 10 mt of wing span).

Again, the local method behaves more uniformly over all basis functions, even in the case of smooth basis functions.

4.3.4 Load Distribution

Even though the conservation of forces and work is guaranteed for each method, an advantage of the local algorithm comes from the local way in which it couples the force fields.

In most cases, global methods result in nonsparse coupling matrices so that using the transposed matrix for ex-

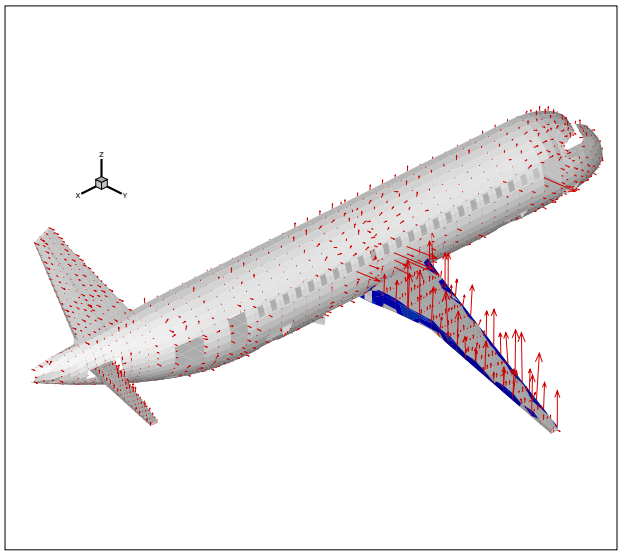

Figure 22 : Transformed forces on the FE model, local method

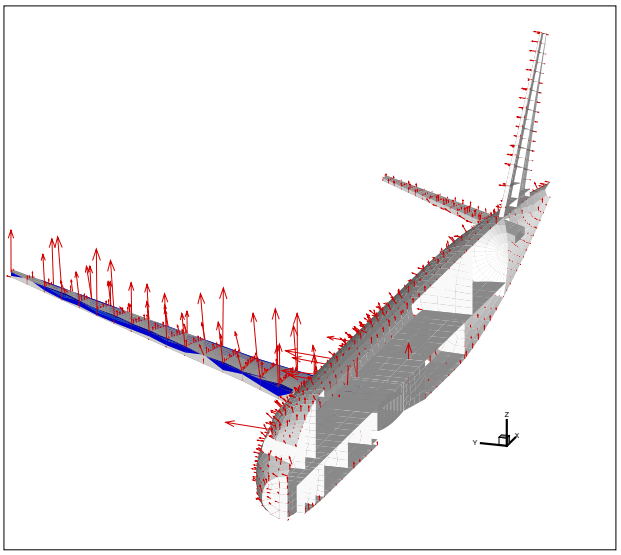

Figure 23 : Transformed forces on the FE model, local method

changing forces will eventually destroy any local character of the force distribution. This leads, in certain cases, to a non-physical distribution of loads. Local methods instead, result in a distribution which is similar to the "physical" one.

As shown in Figures 20, 21 (global) and 22, 23 (PoU), the global coupling algorithm returns a certain number of concentrated high modulus forces, where most of the lift is produced. On the other hand, with the local method high peaks of forces are more uniformly distributed to the leading and trailing edges of the lifting surfaces which is physically more reasonable.

4.3.5 Computational Time

The new local method leads to convergence after 5 iterations with a residual of $\varepsilon = 3.44e^{-4}$. Here, the residual is defined to be the relative difference in displacements of two consecutive solution steps. For comparison, the classical, global spatial coupling approach needed 6 iterations to stop with an even worse residual of $\varepsilon = 1.16e^{-3}$. Figure 24 visualizes the residual over the iteration steps and shows once again the superiority of the local method.

Table 3 shows the different computational times for both methods. The aeroelastic computations have been performed on a Linux workstation cluster, using 8 Intel Xeon 2.66 GHz CPUs. The CFD solution was partitioned into 6 domains and distributed on 6 CPUs, while the structural solution and the coupling algorithm were each computed on one of the remaining CPUs.

It is remarkable that even the time for the CFD solver im-

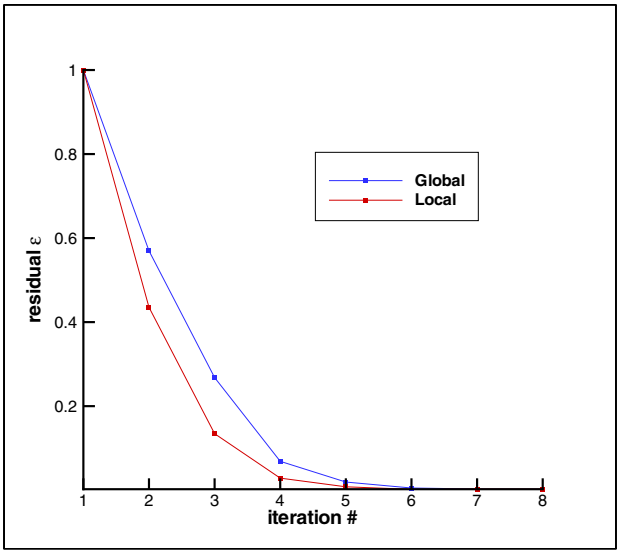

Figure 24 : Convergence of static aeroelastic solution

Table 3 : Computational Time

Times/Method	Global	PoU
Spatial Coupling [sec.]	5000	20
CFD Solution [sec.]	7500	6700
Total [sec.]	12700	7000

proves with the new local method. This is apparently due to the fact that a physically more relevant distribution of forces is obtained by the local method on the structural mesh resulting in more reasonable deformations. The latter produce a better deformation of the aerodynamical mesh resulting also into an improved behavior of the CFD solver.

4.3.6 Boundary Effects

In this subsection, we analyze the effects of the coupling algorithm on the deformation of the wing profile more thoroughly by looking at vertical displacement along chordwise slices. These slices have been sampled at different locations, namely 18%, 50%, 75% and 95%, of the wing span.

Fig. 25 shows a typical behavior of the chordwise displacement encountered in several computations using the global method. Such a displacement pattern is responsible for the deformation of the wing profile. Note that the maximum displacement occurs in a location different from the trailing edge (TE). Since points behind the location of the maximum are subject to a smaller displacement this results in a deformation of the profile. Even if this is feasible it stands in contrast to the design criteria of the specific model, which require the profile shape to be conserved by means of the rib's stiffness. To obtain a rigid rotation, the maximum vertical displacement must be attained at the TE.

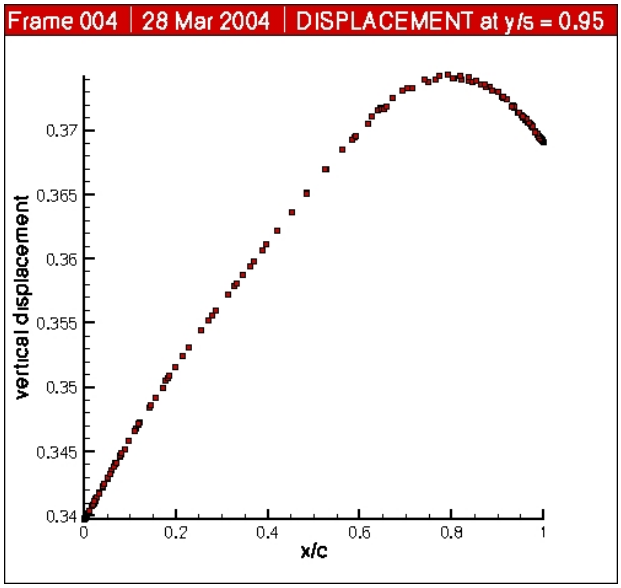

Figure 25 : Chordwise vertical translation pattern

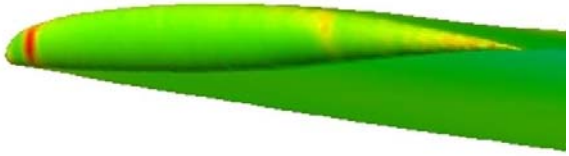

Figure 26 : Real scale deformation.

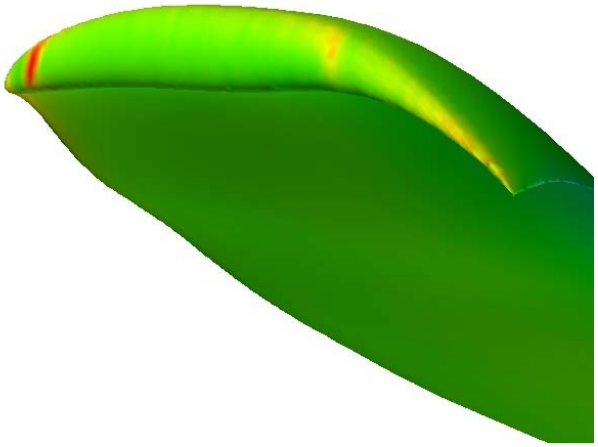

Figure 27 : Real scale deformation, 10 x amplified.

Though evident on the 2D plot, this deformation can be spotted from the 3D representation (Figure 26) only through an amplification by a factor 10 as shown in Figure 27. This demonstrates that the differences in computed displacements are quite small; their order is of fractions of millimeters. However, the increase in the camber of the profile produces an increase in the lift at the rear section of the wing resulting in an increase of the pitching moment.

This phenomenon was encountered only when coupling the meshes by the global method and mainly for the slice

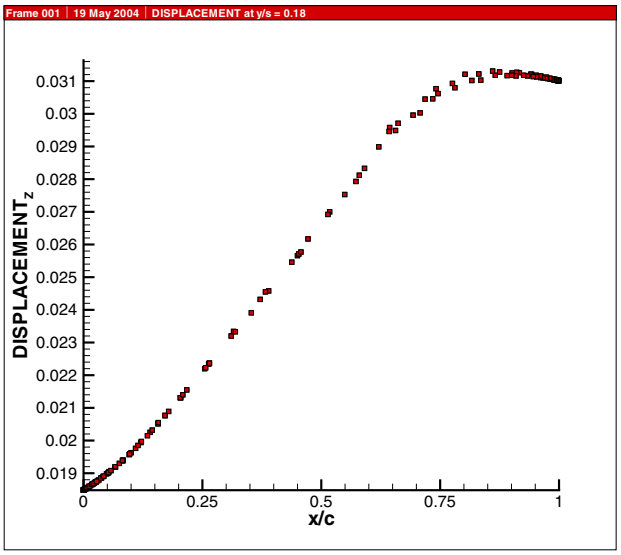

Figure 28 : Chordwise T3, TPS global method, 18% of wing span

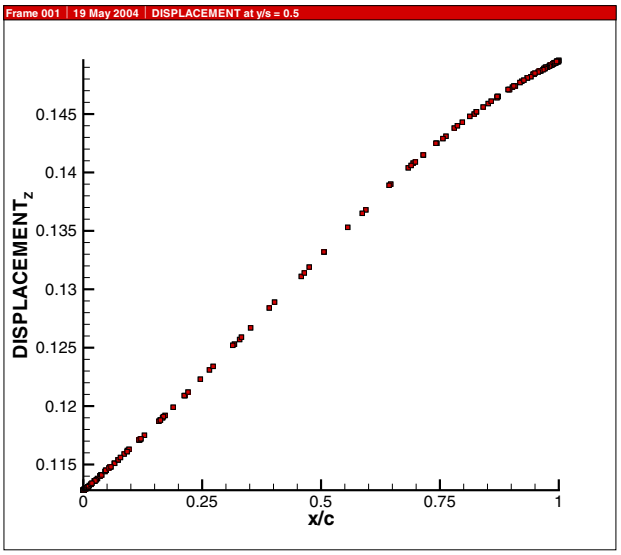

Figure 29 : Chordwise T3, TPS global method, 50% of wing span

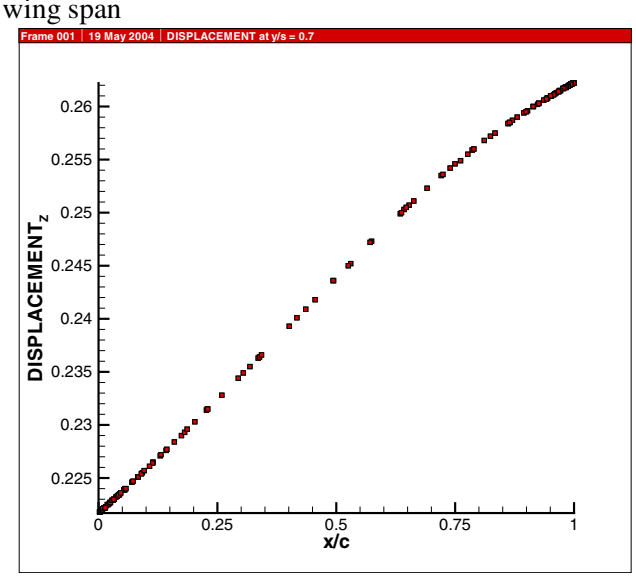

Figure 30 : Chordwise T3, TPS global method, 70% of wing span

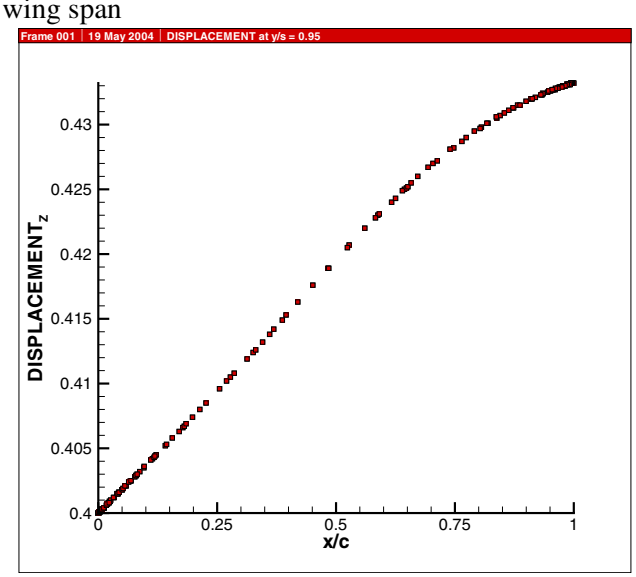

Figure 31 : Chordwise T3, TPS global method, 95% of wing span

at 18% wing span. (see Figures 28 to 31). It seems that this is caused by the global character of the interpolant and the resulting influence of interpolation points from the fuselage.

To eliminate this effect, the influence of different parts of the aircraft has to be minimized. Figures 32 to 35 illustrate that this is automatically achieved by the local method.

Acknowledgement: The results in the fourth section were produced by Filippo Mattioni in Mattioni (2004) using our coupling libraries.

References

Atluri, S. N. (2004): *The Meshless Method(MLPG) for Domain & BIE Discretizations*. Tech Science Press, Forsyth, USA. 680 pages.

Atluri, S. N. (2005): *Methods of Computer Modeling in Engineering & the Sciences, Volume I*. Tech Science Press, Forsyth, USA.

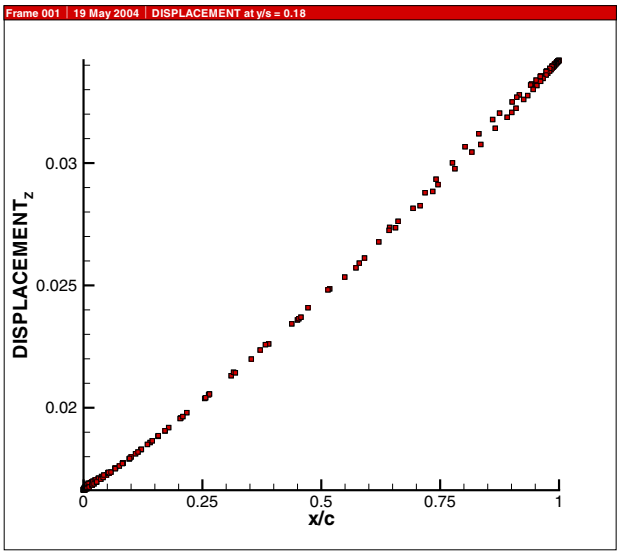

Figure 32 : Chordwise T3, W1 local method, 18% of wing span

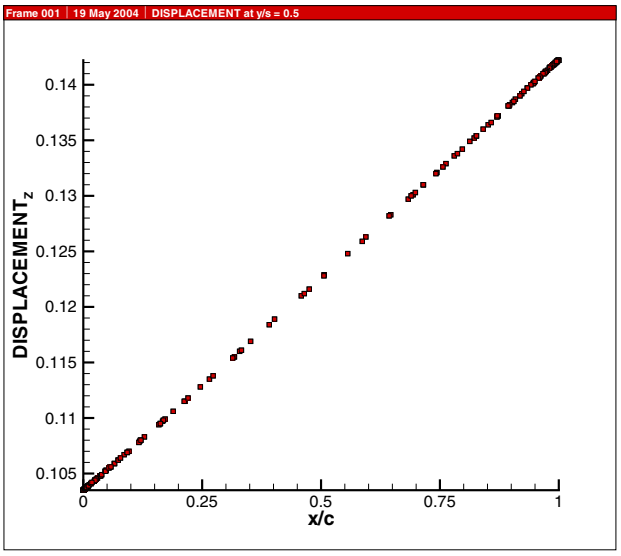

Figure 33 : Chordwise T3, W1 local method, 50% of wing span

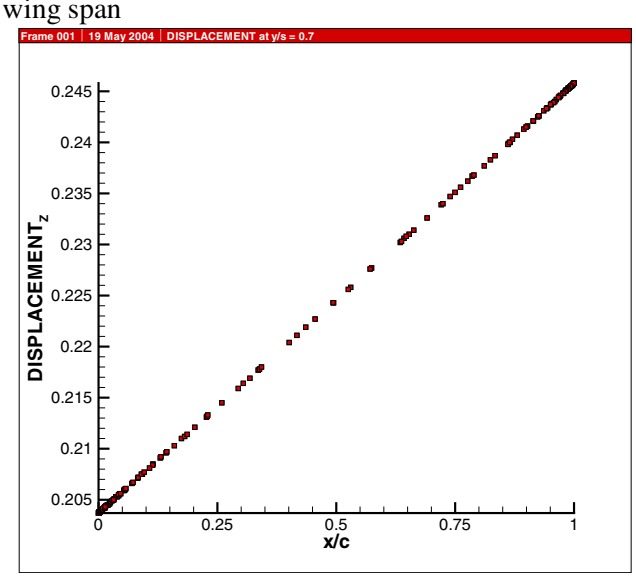

Figure 34 : Chordwise T3, W1 local method, 70% of wing span

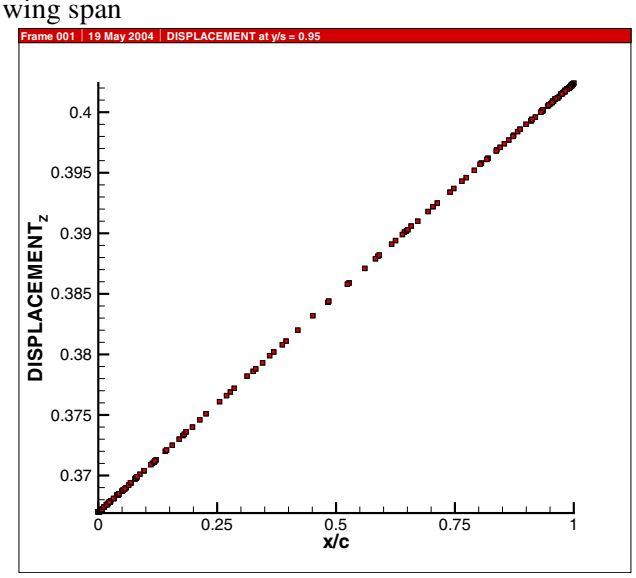

Figure 35 : Chordwise T3, W1 local method, 95% of wing span

Atluri, S. N.; Shen, S. P. (2005): The basis of meshless domain discretization: the meshless local petrov-galerkin (mlpg) method. *Adv. Comput. Math.*, vol. 23, pp. 73–93.

Beckert, A. (2000): Coupling fluid (CFD) and structural (FE) models using finite interpolation elements. *Aerosp. Sci. Technol.*, vol. 1, pp. 13–22.

Beckert, A.; Wendland, H. (2001): Multivariate interpolation for fluid-structure-interaction problems using radial basis functions. *Aerosp. Sci. Technol.*, vol. 5, pp. 125–134.

Bisplinghoff, R. L.; Ashley, H. (1962): *Principles of Aeroelasticity*. John Wiley & Sons, Inc., New York.

Buhmann, M. D. (2001): A new class of radial basis functions with compact support. *Math. Comput.*, vol. 70, pp. 307–318.

Done, G. T. S. (1996): Past and future progress in fixed and rotary wing aeroelasticity. *Aeronautic Journal*, vol. 100, pp. 260–279.

Dowell, E. H.; Crawley, E. F.; Jr., H. C.; Peter, D. A.; Scanlan, R. H.; Sisto, F. (1995): *A Modern Course in Aeroelasticity*. Kluwer Acad. Pub., Dordrecht/Boston.

Edward, J. W. (1993): Computational aeroelasticity. In *Flight-Vehicles, Materials, Structures and Dynamics – Assessment and Future Directions*, volume 5. The American Society of Mechanical Engineers, New York.

Farhat, C.; Lesoinne, M. (1998): Higher-order staggered and subiteration free algorithms for coupled dynamic aeroelasticity problems. In *36th Aerospace Sciences Meeting and Exhibit,AIAA 98-0516, Reno/NV*.

Fornasier, L.; Rieger, H.; Tremel, U.; der Weide, E. V. (2002): Time-dependent aeroelastic simulation of rapid manoeuvring aircraft. In *In 40th AIAA Aerospace Sciences Meeting & Exhibit, 14–17 January 2002, Reno Nevada*. AIAA.

Försching, H. (1974): *Grundlagen der Aeroelastik*. Springer, Heidelberg-Berlin-New York.

Försching, H. (1994): New ultra high capacity aircraft (uhca) - challenges and problems from an aeroelastic point of view. *ZFW*, vol. 18, pp. 219–231.

Försching, H. (1995): Challenges and perspectives in computational aeroelasticity. In *Proc. of the International Forum on Aeroelasticity and Structural Dynamics*, volume 1, pp. 1.1 – 1.9, Manchester (UK).

Fung, Y. C. (1955): *An introduction to the theory of aeroelasticity*. John Wiley, New York.

Geuzaine, P.; Brown, G.; Harris, C.; Farhat, C. (2003): Aeroelastic dynamic analysis of a full f-16 configuration for various flight conditions. *AIAA Journal*, vol. 41, pp. 363–371.

Harder, R. L.; Desmarais, R. N. (1972): Interpolation using surface splines. *Journal of Aircraft*, vol. 9, pp. 189–197.

Hounjet, M. H. L.; Meijer, J. J. (1994): Evaluation of elastomechanical and aerodynamic data transfer methods for non-planar configurations in computational aeroelastic analysis. Technical report, ICAS-Publication, 1994.

MacNeal-Schwendler Corp.. *MSC.Nastran - Handbook for Aeroelastic Analysis I/II*, 1987. ISSN 0741-8043.

Mattioni, F. (2004): Studies on the effects of global and local spatial coupling methods in static aeroelstic analysis. Diploma thesis, Universita Romà "La Sapienza", 2004.

Wendland, H. (2002): Fast evaluation of radial basis functions: Methods based on partition of unity. In Chui, C. K.; Schumaker, L. L.; Stöckler, J.(Eds): *Approximation Theory X: Wavelets, Splines, and Applications*, pp. 473–483, Nashville. Vanderbilt University Press.

Wendland, H. (2005): *Scattered Data Approximation*. Cambridge Monographs on Applied and Computational Mathematics. Cambridge University Press, Cambridge, UK.